ECLÉTICA QUÍMICA

Eclet. Quim. 51 | e-1623, 2026

Original Articles in Chemistry and Related Areas

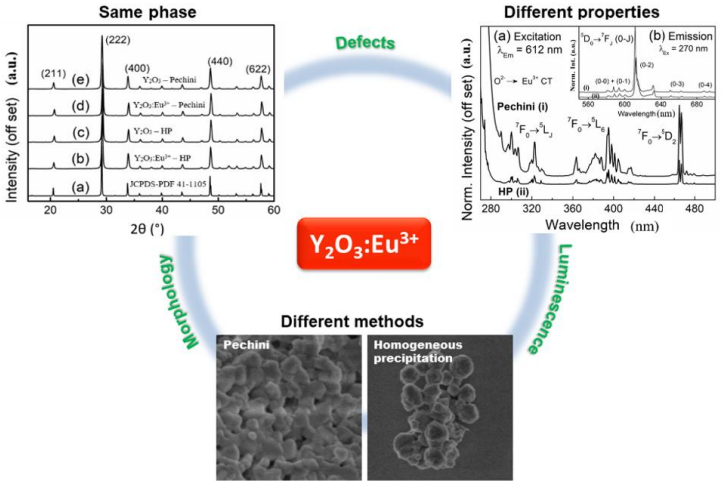
https://doi.org/10.26850/1678-4618.eq.v51.2026.e1623

# UV and X-ray excited optical luminescence of $Y_2O_3:Eu^{3+}$: A correlation of microstructural parameters and its spectroscopic properties

Maike de Oliveira **Krauser**[1,2], Higor Henrique de Souza **Oliveira**[1,3], Marco Aurélio **Cebim**[1+], Marian Rosaly **Davolos**[1]

## Abstract

This paper describes the microstructure, luminescence, and scintillation of nominally pure and 1.0 at.% $Eu^{3+}$-doped $Y_2O_3$ prepared using two distinct chemical methods: (i) Pechini and (ii) homogeneous precipitation method. The microstructure of the materials was studied by calculating the Scherrer crystallites and Williamson–Hall parameters derived from powder X-ray diffraction data. Both methods operated under similar thermal and atmospheric conditions, producing particles with diameters within the same range. Considering that this size regime was probably slightly influenced by quantum confinement effects, it was possible to correlate changes in crystallite sizes and lattice distortion with the relative concentration of defects in each sample and analyze its impact on the $Eu^{3+}$ emission lines, $O^{2-} \rightarrow Eu^{3+}$ charge transfer band, and emission intensity from excitation by X-rays. The defects considered here were not restricted to vacancies and interstitial species, which are commonly cited in rare earth sesquioxides. Still, they include surface species, such as hydroxyl, carbonyl, and carbonate groups, which are derived from the decomposition of precursor materials in each preparation method.




### Article History

Received February 06, 2025
Accepted June 10, 2025
Published November 18, 2026

### Keywords

1. luminescence
2. charge-transfer
3. microstructural parameters
4. chemical synthesis
5. scintillation

### Section Editors

Rogéria Rocha Gonçalves

### Highlights

- Microstructural parameters of Y2O3 and Y2O3:Eu3+ as a function of synthetic routes.
- Relation of microstructural parameters with luminescent and scintillation properties.
- X-ray excited optical luminescent measurements to evaluate scintillation properties.

[1] Univerersidade Estadual Paulista, Instituto de Química, Araraquara, Brazil. [2]Universidade Federal do Tocantins, Química Ambiental, Gurupi, Brazil. [3]Instituto Federal de Educação, Ciência e Tecnologia de São Paulo, Matão, Brazil. **+Corresponding author:** Marco Aurélio Cebim, **Phone:** +551633019595, **Email address:** marco.cebim@unesp.br

creative commons

# 1. Introduction

In the past decade, the preparation and characterization of rare earth sesquioxide nanoparticles have been the subject of several studies (Boukerika and Guerbous, 2014; Chen *et al.*, 2014; Khachatourian *et al.*, 2016; Khan *et al.*, 2020; 2018; Lu *et al.*, 2013; Malek Khachatourian *et al.*, 2015; Park *et al.*, 2017; Yousif *et al.*, 2020). Compared to bulk materials, nanometric structures may exhibit different spectroscopic properties, which are closely tied to the crystalline structure and particle morphology (Joffin *et al.*, 2005; Wang *et al.*, 2007).

Yttrium sesquioxide can be used as a suitable inorganic host for doping with trivalent lanthanides ($Ln^{3+}$) because this process is an isovalent substitution ($Y^{3+} \rightarrow Ln^{3+}$), in which the ionic radii difference is not pronounced, and both elements exhibit similar electronegativities. Furthermore, trivalent yttrium compounds do not exhibit luminescence (bands or lines) in the visible region of the electromagnetic spectrum at room temperature (Blasse and Grabmaier, 1994).

Rare earths have been considered optical materials, and a property of interest is scintillation (Dujardin *et al.*, 2018). These materials are used in radiation detection and nuclear spectroscopy (Ahmadov *et al.*, 2021), medical imaging (Ezirmik, 2021), and ionizing radiation detection, such as in the production of singlet oxygen ($^1O_2$) in X-ray-induced photodynamic therapy (X-PTD) (Zhou *et al.*, 2018).

Thus, $Y_2O_3$ can be used to prepare several doped compounds with different optical properties. Doping with different trivalent lanthanide cations produces materials with different luminescent properties; for instance, the addition of $Tb^{3+}$ to $Y_2O_3$ results in a green light phosphor (Khan *et al.*, 2018), while co-doping with $Er^{3+}$ and $Yb^{3+}$ can produce a luminescent up-conversion phosphor (Tomala and Strek, 2020).

Different methods have been applied to obtain $Y_2O_3$ and $Y_2O_3$:$Ln^{3+}$ nanocrystals, such as microemulsion preparation (Wu *et al.*, 2010), spray pyrolysis (Joffin *et al.*, 2005), polymeric precursor method (Ferrari *et al.*, 2010), and homogeneous precipitation (HP) in aqueous (Pires *et al.*, 2001) and nonaqueous solutions (Sun *et. al.*, 2004). $Eu^{3+}$-doped $Y_2O_3$ compounds have been extensively studied, and their spectroscopic properties are related to the intraconfigurational $4f^6 \rightarrow 4f^6$ transitions of $Eu^{3+}$ ions. In particular, the emission lines in the wavelength range of 550–800 nm for $Y_2O_3$:$Eu^{3+}$ materials were assigned to $^5D_0 \rightarrow {}^7F_J$ (J = 0–4) transitions, and this set of lines can be used as a structural guideline to study the chemical environment around $Eu^{3+}$ ions (Pires *et al.*, 2001).

Oppositely, the excitation spectra of $Y_2O_3$:$Eu^{3+}$ may present $Eu^{3+}$ absorption lines assigned to 4f–4f intraconfigurational transitions (from $^7F_0$ fundamental state to excited levels) and broad bands attributed to valence band to conduction band transitions (VB → CB) in the $Y_2O_3$ and oxygen to metal ($O^{2-} \rightarrow Eu^{3+}$) charge-transfer (CT) process. The excitation from an $O^{2-} \rightarrow Eu^{3+}$ CT depends on the ionicity and electronegativity of the $Eu^{3+}$ chemical environment, $Eu^{3+}$ coordination number, and O–Eu distances (Dorenbos, 2005).

This study analyzed the influence of two different preparation pathways, i.e., the (i) polymeric precursor method (Pechini, 1967) and (ii) HP in an aqueous solution (Gaspar *et al.*, 2010) on the microstructural properties, such as the Scherrer's crystallite size and Williamson–Hall parameters of $Y_2O_3$ and $Y_2O_3$:$Eu^{3+}$ 1.0 at.%. The observed tendencies on the microstructural parameters correlated with the luminescence and scintillation of these materials. Methods (i) and (ii) were chosen because (i) it is possible to obtain nanoparticles without shape and size control, in contrast to (ii), where it is possible to prepare spherical particles with a narrow size distribution. This study evaluated the effect of the crystallinity and relative defect concentration on the luminescence of $Y_2O_3$:$Eu^{3+}$ 1.0 at.%, such as the $O^{2-} \rightarrow Eu^{3+}$ charge transfer (CT) process and the $Eu^{3+}$ emission spectral profiles obtained from excitation by ultraviolet and X-rays.

# 2. Materials and methods

Nominally pure and 1.0 at.% $Eu^{3+}$-doped $Y_2O_3$ were prepared using the Pechini method (polymeric precursor method) (Pechini, 1967) and a modified HP method in an aqueous solution (Gaspar *et al.*, 2010). We used $Y_2O_3$ and $Eu_2O_3$ (Sigma-Aldrich, 99.999%) as starter reagents for both methods. All other reagents were of analytical grade. Using the Pechini method, aqueous solutions of $Y(NO_3)_3$ and $Eu(NO_3)_3$ at defined proportions were poured into a beaker containing citric acid (CA) at a molar ratio of 1:3 (metal:CA). The pH of the resulting solution was adjusted to 5.0 with a 0.1 mol $L^{-1}$ $NH_4OH$ solution and stirred for 1 h. Afterwards, ethylene glycol (EG) was added to the solution at a molar ratio of 1:16 (metal:EG) and heated (~ 100 °C) until a yellowish polymeric resin was formed and thermally treated in a tubular furnace in a static air atmosphere at 1100 °C for 4 h. Using the HP method, 250 mL of the $Y(NO_3)_3$ aqueous solution ($3.0 \times 10^{-3}$ mol $L^{-1}$) was mixed with 15.0 g of urea in a round-bottom flask. After the urea dissolved, the resulting solution was placed in a water bath at 80 °C for 2 h under rotation in a rotary evaporator. To prepare the $Eu^{3+}$-doped sample, the $Y(NO_3)_3$ solution was replaced with an aqueous solution of $Y_{0.99}Eu_{0.01}(NO_3)_3$ ($3.0 \times 10^{-3}$ mol $L^{-1}$). The obtained white precipitate was filtered under reduced pressure and washed with distilled water. The powder was dried in a desiccator and thermally treated in a tubular furnace in a static air atmosphere at 1100 °C for 4 h.

The samples were characterized by powder X-ray diffraction (XRD) with Cu $K_\alpha$ radiation ($\lambda$ = 1.5442 Å) using a Rigaku Rint 2000/PC diffractometer operating at 42 kV and 120 mA. The data were collected in the $2\theta/\theta$ mode within the 3–120° range at a 0.02/2 s propagation step. The particle shape and size were analyzed using a field-emission gun scanning electron microscope (FEG-SEM) with a Jeol JSM 7500F operating at 2 kV and equipped with a secondary electron detector. Fourier transform infrared (FT-IR) spectroscopy was performed in the 400–4000 $cm^{-1}$ wavenumber range using a PerkinElmer Spectrum 2000 spectrometer with sample/KBr pellets. To evaluate the luminescence, excitation and emission spectra were recorded using photoluminescence spectroscopy (PLS) with a SPEX Fluorlog 2 fluorimeter, equipped with a 450 W xenon lamp, a double monochromator, and a Hamamatsu photomultiplier. The radio luminescent properties were investigated using X-ray excited optical luminescence (XEOL) measurements, where copper X-ray excitation was generated by a homemade X-ray generator operating at 40 kV and 20 mA. The luminescent response was recorded using an iDus DV401A-BV CCD camera (Andor Technology) coupled with a SHAMROCK 163 spectrometer (Andor Technology) (Cebim *et al.*, 2011).

# 3. Results and discussion

## 3.1. X-ray diffraction (XRD)

The XRD patterns of the samples prepared using both methods are shown in **Fig. 1**. All the samples exhibited the same diffraction pattern, assigned to a fully crystalline single phase of yttrium oxide with a cubic crystalline structure and space group, $I_{a3}$ (JCPDS PDF Card Nº 41-1105). The diffraction peaks were

used to evaluate the crystallite size ($D_S$) using the Scherrer **Eq. 1** as follows:

$$D_S = \frac{K\lambda}{\sqrt{(\beta_{hkl})^2_{measured} - (\beta)^2_{instrumental}}\cos\theta_{hkl}} \quad (1)$$

where $\lambda$ is the X-ray wavelength (1.5406 Å), $\beta$ is the full width at half maximum (FWHM), $\theta_{hkl}$ is the Bragg angle of the *hkl* peak, and $K$ is a shape constant equal to 0.89. For the Williamson–Hall calculations, the crystallite size ($D_{WH}$) and lattice distortion (strain, $\varepsilon$), depending on the crystal direction, were evaluated with **Eq. 2**:

$$\beta_{hkl}\cos\theta_{hkl} = \frac{K\lambda}{D_{WH}} + 2\varepsilon\sin\theta_{hkl} \quad (2)$$

where $K$ and $\lambda$ are the same parameters used in the Scherrer **Eq. 1**.

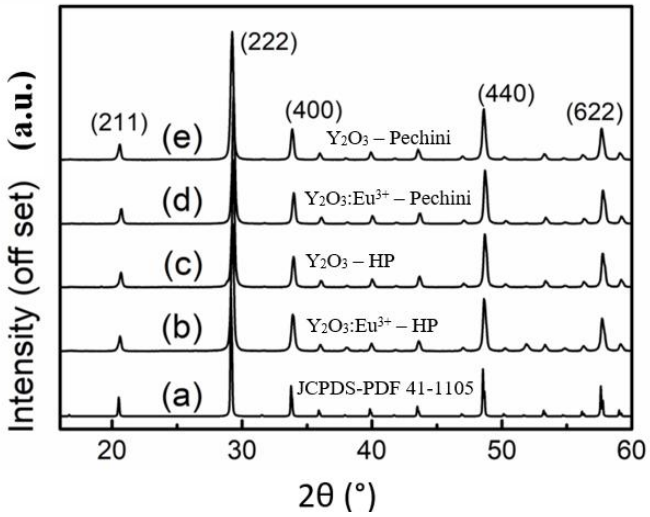



**Figure 1.** X-ray diffraction data of the $Y_2O_3$ and $Y_2O_3$:$Eu^{3+}$ 1.0 at.% samples obtained using the Pechini and homogeneous precipitation (HP) methods.
**Source**: Elaborated by the authors.

The data obtained using **Eqs. 1** and **2** are listed in **Table 1** (samples obtained using the Pechini method) and **Table 2** (samples obtained using the HP method). These defects shifted the diffraction peaks by a few degrees from their original positions by creating extended and point defects in the material lattice, thereby modifying the crystallite sizes and lattice distortion. Rare-earth sesquioxides commonly present oxygen vacancies along with interstitial species (Levy *et al.*, 2007; Stanek *et al.*, 2008).

The crystallite sizes determined by the Scherrer equation differed from those determined by the Williamson–Hall calculations. When the Scherrer equation is used to assess crystallite size, a single diffraction peak of one (hkl) plane is used. For Williamson–Hall calculations, each crystallite size is determined using a set of diffraction peaks related to a set of (hkl) planes.

For the nominally pure and 1.0 at.% $Eu^{3+}$-doped $Y_2O_3$ samples prepared using the Pechini method, **Table 1** shows that the crystallite sizes obtained by the Scherrer equation were generally lower than those obtained by the Williamson–Hall calculations. For the $Y_2O_3$:$Eu^{3+}$ sample, the lattice distortion was higher for the nominally pure sample at the (h22) and (2k0) planes, as observed in the strain values. However, doping decreased the lattice distortion compared with the nominally pure oxide for the set of (h11) planes.

No trend was observed for the crystallite sizes of the samples prepared via HP, regardless of the calculation method. As observed in the crystallite sizes calculated for the $Y_2O_3$:$Eu^{3+}$ 1.0 at.% obtained using the Pechini method, the lattice distortion of the doped sample prepared by HP was higher than that of the nominally pure sample for two sets of planes, h11 and 4k0, nevertheless, for different plane sets. Therefore, the distortion of the planes by doping was not uniform in these materials.

Crystal structure distortions, i.e., unity cells or lanthanide sites with distorted bond distances (Ln–O), are related to the relative amount of structural defects (Adachi *et al.*, 2004). The highest lattice distortions observed in the $Eu^{3+}$-doped samples prepared using both methods were possibly related to the ionic radii difference between the $Y^{3+}$ and $Eu^{3+}$ ions and consequently to the high relative concentration of structural defects in the doped samples. However, the Scherrer and Willamson–Hall calculations indicated a smaller concentration of defects in the nominally pure samples than in the $Y_2O_3$:$Eu^{3+}$ samples.

In general, the crystallite sizes obtained by the Scherrer equation were higher for the samples prepared by HP, as observed in **Table 1** and **2**. Furthermore, the lattice distortions of the samples prepared by HP were low, compared with the strain values of the samples prepared using the Pechini method. Therefore, HP appeared to yield particles with higher crystallinity, compared with those obtained using the Pechini method under the same thermal treatment conditions (temperature and atmosphere).

Srinivasan *et al.* (2010) employed the Williamson–Hall method to determine the microstructural parameters of $Y_2O_3$ and $Y_2O_3$:$Eu^{3+}$ samples prepared by the coprecipitation method. They evaluated the effect of the thermal treatment and particle size on the $D$ and $\varepsilon$ values. They observed that a sample treated at 800 °C exhibited a smaller distortion and higher crystallite size, compared with that treated at 500 °C. Additionally, the $D$ values obtained from the Williamson–Hall calculations were approximately equal to those obtained from the Scherrer equation.

Microstructural distortions were observed for the $Y_2O_3$ samples prepared using different methods. For the doped samples, the presence of the dopant modified nature and relative concentration of defects. Notably, other preparation methods follow different chemical pathways, leading to a specific "history" of chemical transformations, which are generally imprinted in the samples as extended or point defects. In addition, by comparing the crystallite sizes and lattice distortions of the crystallographic planes, the structural parameter calculation indicated a higher defect concentration in the samples prepared using the Pechini method compared to those prepared by HP.

The lattice constant, ***a***, was estimated from the X-ray diffraction data shown in **Fig. 1**, and the obtained values are shown in **Table 3**. For the HP method, the insertion of $Eu^{3+}$ ions did not significantly affect ***a***. However, for the Pechini method, the $Eu^{3+}$ dopant ions changed the lattice parameter from 10.75 to 10.91 Å, likely because this method provided a higher number of defects in the crystal structure compared to the HP method.

**Table 1.** Crystallite sizes and strain lattices of $Y_2O_3$ and $Y_2O_3$:$Eu^{3+}$ obtained using the Pechini method.

| Sample | hkl | Position 2θ (°) | FWHM Δ(2θ) (°) | Scherrer Crystallite size $D_S$ (nm) | Williamson–Hall Crystallite size $D_{WH}$ (nm) | Strain |
|---|---|---|---|---|---|---|
| $Y_2O_3$ | h22 | | | | 41.2 | 0.0020 |
| | 222 | 29.36 | 0.24098 | 15.1 | | |
| | 622 | 57.80 | 0.32159 | 33.4 | | |
| $Y_2O_3$ | *h*11 | | | | 49.1 | 0.0037 |
| | 211 | 20.74 | 0.23768 | 38.0 | | |
| | 411 | 36.12 | 0.26046 | 30.7 | | |
| | 611 | 53.38 | 0.29632 | ----- | | |
| $Y_2O_3$ | 4*k*0 | | | | 49.5 | 0.0034 |
| | 400 | 33.98 | 0.24547 | 30.5 | | |
| | 440 | 48.70 | 0.28320 | 14.5 | | |
| $Y_2O_3$:$Eu^{3+}$ | h22 | | | | 45.1 | 0.0032 |
| | 222 | 29.24 | 0.25036 | 44.3 | | |
| | 622 | 57.68 | 0.32486 | 32.6 | | |
| $Y_2O_3$:$Eu^{3+}$ | *h*11 | | | | 42.8 | 0.0024 |
| | 211 | 20.60 | 0.24084 | 46.8 | | |
| | 411 | 36.00 | 0.25053 | 45.0 | | |
| | 611 | 53.26 | 0.30663 | 34.7 | | |
| $Y_2O_3$:$Eu^{3+}$ | 4*k*0 | | | | 47.8 | 0.0036 |
| | 400 | 33.88 | 0.25509 | 43.3 | | |
| | 440 | 48.62 | 0.29474 | 36.0 | | |

**Source**: Elaborated by the authors.

**Table 2.** Crystallite sizes and strain lattices of $Y_2O_3$ and $Y_2O_3$:$Eu^{3+}$ obtained using the homogeneous precipitation method.

| Sample | hkl | Position 2θ (°) | FWHM Δ(2θ) (°) | Crystallite size Scherrer method (nm) | Crystallite size Williamson–Hall method (nm) | Strain |
|---|---|---|---|---|---|---|
| $Y_2O_3$ | h22 | | | | 44.7 | 0.0031 |
| | 222 | 29.28 | 0.25088 | 44.1 | | |
| | 622 | 57.72 | 0.32427 | 32.7 | | |
| $Y_2O_3$ | *h*11 | | | | 39.1 | 0.0015 |
| | 211 | 20.60 | 0.24404 | 45.7 | | |
| | 411 | 36.02 | 0.25726 | 42.9 | | |
| | 611 | 53.32 | 0.29901 | 36.0 | | |
| $Y_2O_3$ | 4*k*0 | | | | 30.5 | 0.0013 |
| | 400 | 33.92 | 0.27893 | 37.3 | | |
| | 440 | 48.62 | 0.28269 | 38.4 | | |
| $Y_2O_3$:$Eu^{3+}$ | h22 | | | | 46.3 | 0.0030 |
| | 222 | 29.34 | 0.24287 | 46.9 | | |
| | 622 | 57.76 | 0.31425 | 34.2 | | |
| $Y_2O_3$:$Eu^{3+}$ | *h*11 | | | | 43.7 | 0.0026 |
| | 211 | 20.70 | 0.23567 | 48.9 | | |
| | 411 | 36.06 | 0.25346 | 44.0 | | |
| | 611 | 53.38 | 0.30344 | 35.2 | | |
| $Y_2O_3$:$Eu^{3+}$ | 4*k*0 | | | | 46.5 | 0.0028 |
| | 400 | 33.96 | 0.24822 | 45.5 | | |
| | 440 | 48.70 | 0.28192 | 38.5 | | |

**Source**: Elaborated by the authors.

**Table 3.** Lattice constant, ***a***, of undoped and $Eu^{3+}$-doped $Y_3O_2$ samples.

| Sample | Lattice constant *a* (Å) |
|---|---|
| $Y_2O_3$ (JCPDS - PDF Card Nº 41-1105) | 10.65 |
| **Homogeneous Precipitation Method** | |
| $Y_2O_3$ | 10.78 |
| $Y_2O_3$:$Eu^{3+}$ | 10.76 |
| **Pechini Method** | |
| $Y_2O_3$ | 10.75 |
| $Y_2O_3$:$Eu^{3+}$ | 10.91 |

**Source**: Elaborated by the authors.

The large number of defects in the sample obtained using the Pechini method may be related to the noncrystalline structure of the polymeric precursor. In contrast to the Pechini method, the HP method employs a crystalline precursor (hydroxycarbonate), which is expected to be a material with high crystallinity and low defect concentration (Pires *et al.*, 2003).

### 3.1.1. Scanning electron microscopy (SEM)

The SEM micrographs of the nominally pure and 1.0 at.% $Eu^{3+}$-doped $Y_2O_3$ samples prepared using the Pechini method are shown in **Fig. 2**. The formation of aggregates can be observed, which generally comprise sets of particles within a diameter range of 80–100 nm (mean particle sizes of 79.91 ± 25.20 and 85.69 ± 27.70 nm for $Y_2O_3$ and $Y_2O_3$:$Eu^{3+}$ 1.0 at.%, respectively). The doping process had virtually no effect on the particle shape.

Contrarily, the samples prepared by HP exhibited changes in particle size despite the maintenance of the spherical shape, as shown in **Fig. 3**. The mean diameter of the undoped $Y_2O_3$ particles was 136.31 ± 15.94 and 176.00 ± 27.12 nm for doped samples, showing irregular surfaces.

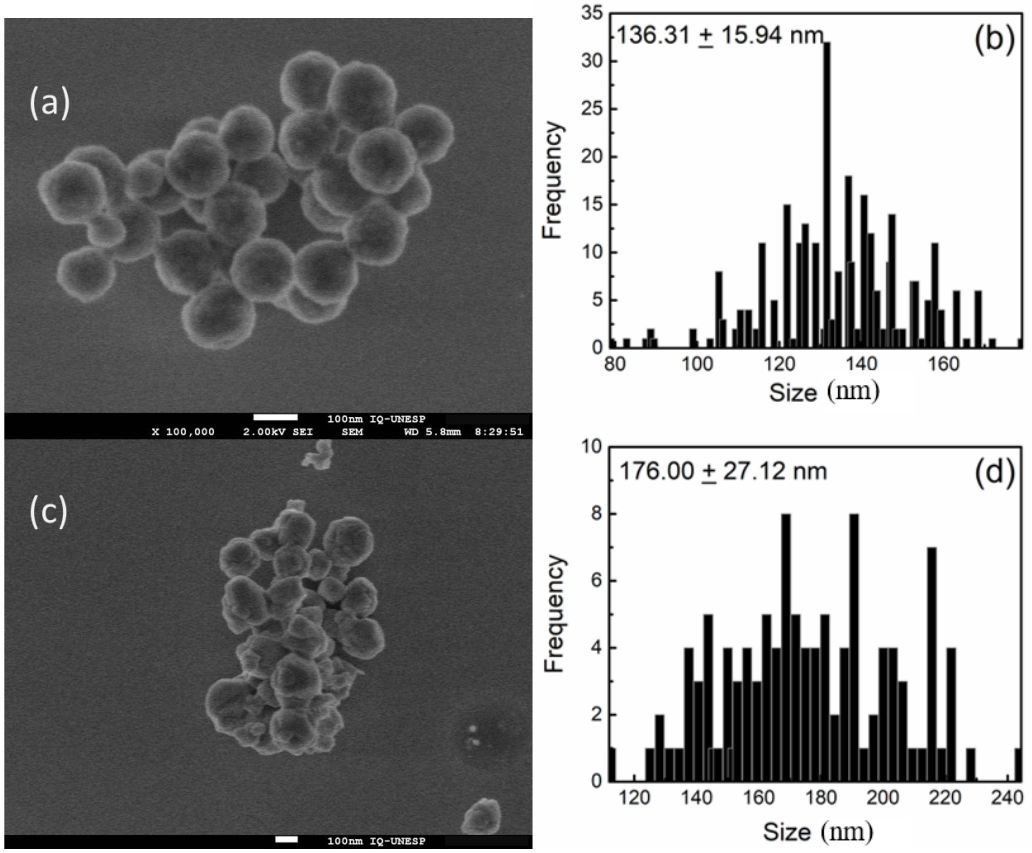



**Figure 2. (a)** Scanning electron microscopy (SEM) results and **(b)** particle size distribution (PSD) of $Y_2O_3$ obtained using the Pechini method. **(c)** SEM results and **(d)** PSD of $Y_2O_3$:$Eu^{3+}$ 1.0 at.% obtained using the Pechini method.
**Source**: Elaborated by the authors.

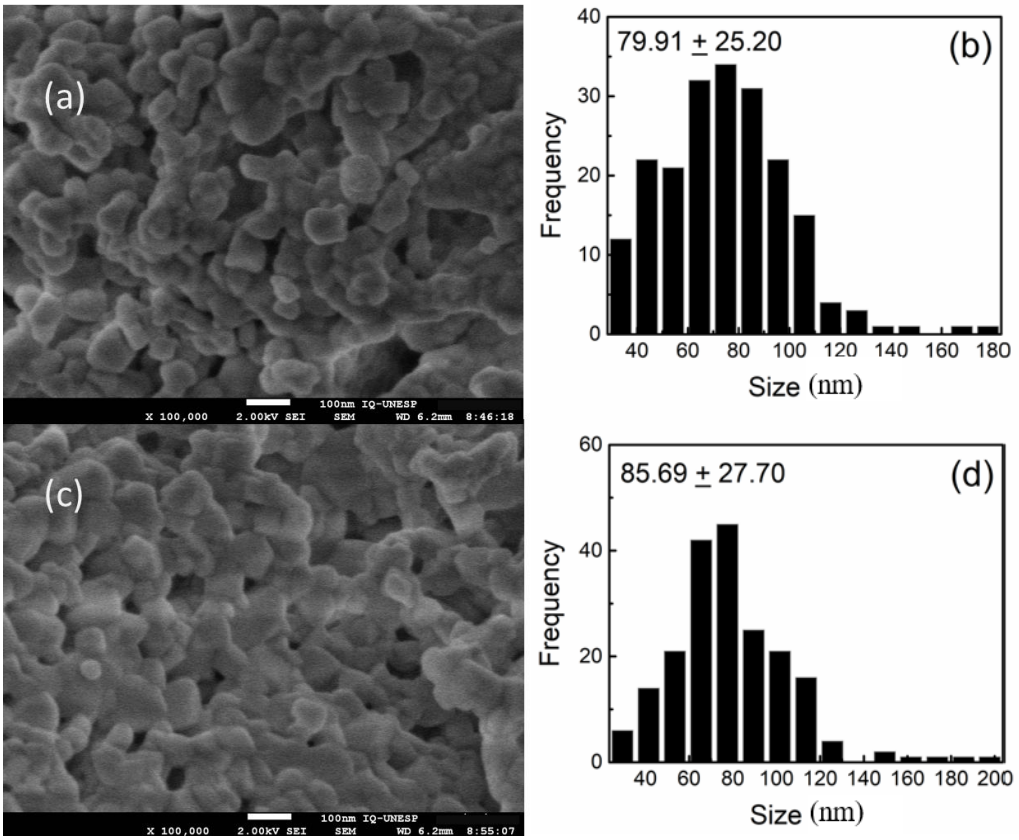



**Figure 3. (a)** Scanning electron microscopy (SEM) results and **(b)** particle size distribution (PSD) of $Y_2O_3$ obtained using the homogeneous precipitation (HP) method. **(c)** SEM results and **(d)** PSD of $Y_2O_3$:$Eu^{3+}$ 1.0 at.% obtained using the HP method.
**Source**: Elaborated by the authors.

### 3.1.2. FT-IR spectroscopy

The FT-IR spectra of the samples are shown in **Fig. 4**. The spectral profiles were somewhat similar for the undoped and 1.0 at.% $Eu^{3+}$-doped samples, with deviations regarding the preparation methods. The principal assignments of vibrational absorptions are shown in **Fig. 4**. They can be summarized as O–H stretching vibrations, H–O–H deformations, symmetric and asymmetric $CO_2$ stretching, C–O stretching, $CO_2$ stretching, carbonate stretching, and metal–oxygen stretching vibrations at 3500, 1635, 1375, 1100, 2355, 655, and a range of 400–750 $cm^{-1}$, respectively (Nakamoto, 2009). The presence of these bands in these compounds is common since the Pechini method is characterized by the thermal decomposition of the organic polymeric precursor, probably leading to the formation of carbonates.

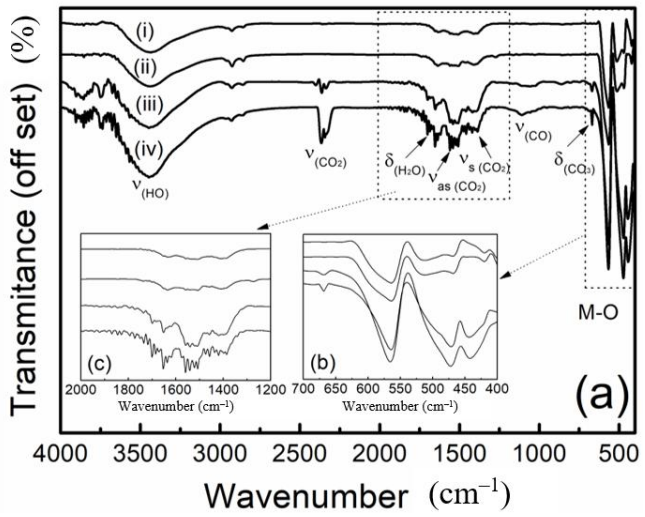



**Figure 4. (a)** Fourier transform infrared spectra of (i) $Y_2O_3$:$Eu^{3+}$ 1% and (ii) $Y_2O_3$ obtained using the Pechini method and (iii) $Y_2O_3$:$Eu^{3+}$ 1% and (iv) $Y_2O_3$ obtained using the homogeneous precipitation method. **(b)** and **(c)** Insets of the regions of 400–700 and 1200–2000 $cm^{-1}$, respectively.
**Source**: Elaborated by the authors.

The bands assigned to carbonyl and carbonate groups were more intense in the samples prepared by HP because, in this synthetic route, the yttrium hydroxycarbonate precursor was thermally decomposed to oxycarbonate and, finally, yttrium oxide (Pires *et al.*, 2001). Therefore, fragments of these carbonate groups can be associated with the particle surface, and they are important in defect formation and charge compensation processes (Levy *et al.*, 2007).

## 3.2. Photoluminescence spectroscopy (PLS)

The emissions spectra of the $Y_2O_3$:$Eu^{3+}$ 1.0 at.% samples are shown in **Fig. 5b**. The emission spectral profiles were the same for both samples. The spectra showed the characteristic emission lines of the $Eu^{3+}$ ion assigned to the $^5D_0 \rightarrow {}^7F_J$ (0-J) transitions, with J varying from 0 to 4. In yttrium oxide, $Eu^{3+}$ ions occupy two different symmetry sites, one of low symmetry ($C_2$) and another of high symmetry (S6) (Buijs *et al.*, 1987). $Eu^{3+}$ ions were present at the $C_2$ sites; therefore, the $^5D_0 \rightarrow {}^7F_2$ emission lines were more intense than those of $^5D_0 \rightarrow {}^7F_1$, as observed in both spectra.

The excitation spectra of the $Y_2O_3$:$Eu^{3+}$ 1.0 at.% samples with an emission wavelength fixed at 612 nm ($^5D_0 \rightarrow {}^7F_2$) are shown in **Fig. 5a**. The lines observed in the 300–500 nm range were assigned to the intraconfigurational transitions of the $Eu^{3+}$ ion and transitions from the $^7F_0$ fundamental level to the excited levels, which were not significantly affected by the preparation method. Part of the $O^{2-} \rightarrow Eu^{3+}$ CT band can be observed, which may be centered approximately within a range of 250–270 nm (Pires *et al.*, 2002; Shang *et al.*, 2011).

Considering that both $Eu^{3+}$-doped $Y_2O_3$ samples were prepared using the same thermal treatment temperature and identical atmospheric conditions and exhibited particle sizes within a similar dimension range, the differences in the CT band energies can be attributed to the different pathways followed by each precursor during the thermal decomposition and consequently to changes at the microstructural level.

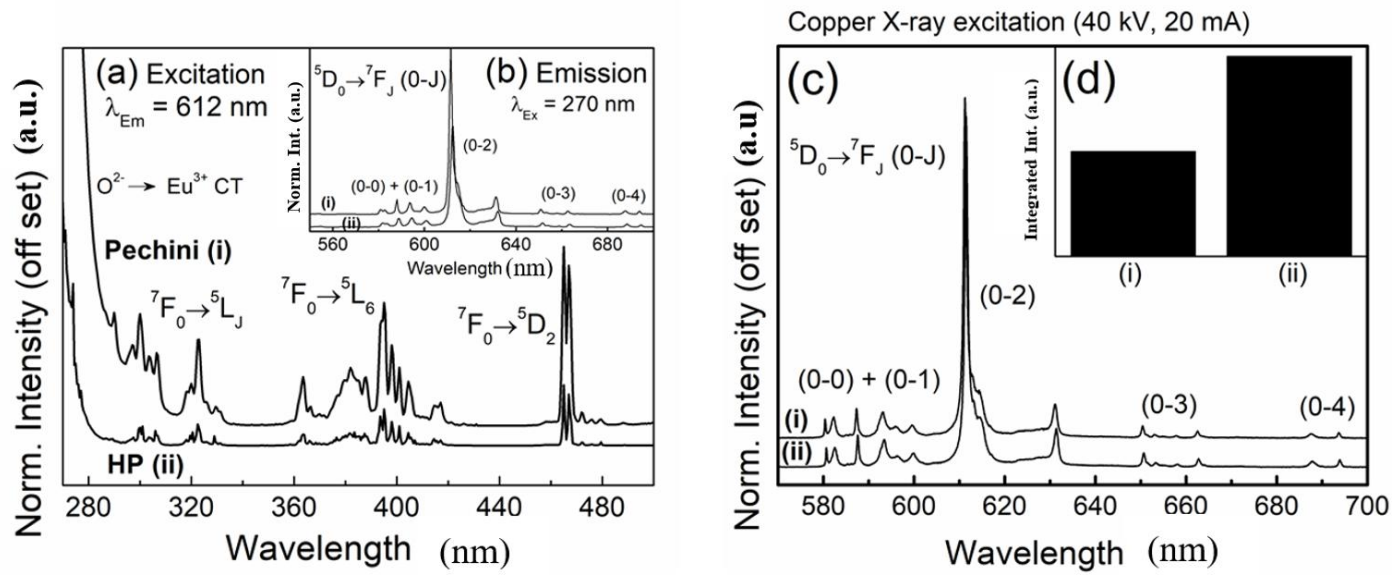



**Figure 5.** Photoluminescence spectra recorded at room temperature of $Y_2O_3$:$Eu^{3+}$ obtained using the (i) Pechini and (ii) homogeneous precipitation (HP) methods: **(a)** excitation spectrum with 612 nm emission and **(b)** emission spectra with 270 nm excitation. **(c)** X-ray excited optical luminescence spectra recorded at room temperature with copper X-ray excitation (40 kV, 20 mA). **(d)** $^5D_0 \rightarrow {}^7F_2$ (0-2) integrated emission intensity of $Y_2O_3$:$Eu^{3+}$ 1.0 at.% obtained using the (i) Pechini and (ii) HP methods.
**Source**: Elaborated by the authors.

The energy position of the CT band ($E^{CT}$) was initially described by Jörgensen (Jørgensen, 1971) using empirical arguments, which can be summarized in Eq. 3:

$$E^{CT} = 3.72\left(\chi_{opt}(X) - \chi_{opt}(M)\right) eV \quad (3)$$

where $\chi_{opt}(X)$ is the optical electronegativity of the $X$ anion (chemical species that donates electron), and $\chi_{opt}(M)$ is the optical electronegativity of the acceptor metallic cation (chemical species that accept electrons from $X$). Dorenbos (2003) described an $E^{CT}$ involving trivalent rare-earth cations as a function of the valence band top and the position of the $Ln^{3+}$ excited state in the forbidden band of the material, as well as the size of the site occupied by $Ln^{3+}$. In general, defects can change the density of states and energy positions of the valence and conduction bands, leading to shifts in the $E^{CT}$.

Shang *et al.* (2011) described a redshift of the $O^{2-} \rightarrow Eu^{3+}$ CT band in $Y_2O_3$:$Eu^{3+}$ nanoparticles due to defects that modify the electronic levels of the material. Remarkably, in the same material, different Eu–O bonds resulting from point defects can alter the CT band position. In particular, charge compensation between the $Eu^{3+}$ dopant and cations of the host matrix can retain anions from the precursor or decomposition of these anions, leading to different Eu–O interactions and consequently, CT band shifting (Pires *et al.*, 1997).

The presence of defects is directly related to the crystallinity and microstructure, influencing the luminescence of Eu3+-doped yttrium oxide material (Mukherjee *et al.*, 2008). Although both samples exhibited similar crystalline properties, the CT band in the excitation spectrum of the sample prepared by HP (ii) exhibited a red shift compared with the CT band of the sample prepared using the Pechini method (i). This suggests that $E^{CT}$ is related to the nature of the electronic defects and the crystalline parameters.

### 3.2.1. X-ray excited optical luminescence (XEOL)

The scintillation was investigated using XEOL, and the emission spectra of $Y_2O_3$:$Eu^{3+}$ 1 at.% are shown in Fig. 5c. The spectra exhibited all the $^5D_0 \rightarrow {}^7F_J$ transitions (with J = 0–4) of $Eu^{3+}$ ions, the lines assigned to the $^5D_0 \rightarrow {}^7F_0$ transition indicated $S_6$ and $C_2$ symmetry sites. The emission profile was like that obtained during the PLS measurements. Although the samples exhibited the same emission spectral profile, we observed that the integrated intensities of the samples differed for each preparation method, as shown in Fig. 5d. The nanoparticles obtained by HP exhibited a higher emission intensity than those obtained using the Pechini method.

Finally, the scintillation efficiency, $\eta$, can be written as Eq. 4:

$$\eta = \beta S Q \quad (4)$$

where $\beta$ and $S$ are the efficiencies related to the radiation absorption and energy transfer processes, respectively. Furthermore, $Q$ is the quantum efficiency of the luminescent center (Blasse, 1994; Zhou *et al.*, 2020).

For the $Y_2O_3$:$Eu^{3+}$ material, $\beta$ and $Q$ were similar for both methods because the phase, composition, and luminescent center were the same. However, the energy transfer process ($S$) can be different because the $e^-/h^+$ pair can be captured for any defects in the lattice or surface.

Therefore, the luminescent intensity can change with concentration of point and extended defects. In this case, we could conclude that the nanoparticles obtained by HP exhibited fewer defect concentrations than those obtained using the Pechini method.

## 4. Conclusions

This study compares the structural (crystallite sizes and lattice distortions) and luminescent properties of nominally pure and 1.0 at.% $Eu^{3+}$-doped $Y_2O_3$ prepared using the Pechini and HP methods. The Scherrer and Williamson–Hall parameters obtained from the X-ray diffraction data indicated that the powders prepared using the Pechini method exhibited a higher relative defect concentration than those prepared by HP. These defects, which included vacancies and interstitial species, were commonly present in lanthanide sesquioxides and likely derived from the specific chemical pathways associated with each preparation method. The FT-IR results revealed the presence of surface groups, including hydroxyl, carbonyl, and carbonate groups. The correlation between the structural parameters and luminescence spectra showed a strong influence of the $Eu^{3+}$ environment on the $O^{2-} \rightarrow Eu^{3+}$ CT band energy and scintillation properties. Following this study, questions regarding the nature of these defects and their impact in $Eu^{3+}$ environments, as well as the electronic structure of the materials, will arise and shed light on the structural properties and their influence on the luminescence efficiency of materials prepared using different methods.

## Authors' contribution

**Conceptualization**: Maike de Oliveira Krauser; Marco Aurélio Cebim; Marian Rosaly Davolos; **Data curation**: Maike de Oliveira Krauser; Marco Aurélio Cebim; **Formal Analysis**: Maike de Oliveira Krauser; Higor Henrique de Souza Oliveira; Marco Aurélio Cebim; **Funding acquisition**: Marco Aurélio Cebim; Marian Rosaly Davolos; **Investigation**: Maike de Oliveira Krauser; Higor Henrique de Souza Oliveira; Marco Aurélio Cebim; **Methodology**: Maike de Oliveira Krauser; Higor Henrique de Souza Oliveira; Marco Aurélio Cebim; Marian Rosaly Davolos; **Project administration**: Marco Aurélio Cebim; Marian Rosaly Davolos; **Resources**: Marian Rosaly Davolos; **Software**: Marco Aurélio Cebim; **Supervision**: Marco Aurélio Cebim, Marian Rosaly Davolos; **Validation**: Marco Aurélio Cebim; **Visualization**: Not applicable; **Writing – original draft**: Maike de Oliveira Krauser; Marco Aurélio Cebim; **Writing – review & editing**: Marco Aurélio Cebim.

## Conflict of interest

The authors declare that they have no known competing financial interests or personal relationships that could have appeared to influence the work reported in this paper.

## Data availability statement

The data will be available upon request.

## Artificial Intelligence usage statement

The authors declare that they did not use Artificial Intelligence tools at any stage of the preparation, correction, or evaluation of this work.

## Funding

Not applicable.

## Acknowledgments

Not applicable.

## References


Adachi, G.; Imanaka, N.; Kang, Z. C. *Binary Rare Earth Oxides*; Adachi, G., Imanaka, N., Kang, Z. C., Eds.; Springer Netherlands: Dordrecht, 2004. https://doi.org/10.1007/1-4020-2569-6

Ahmadov, G.; Ahmadov, F.; Holik, M.; Berikov, D.; Sadygov, Z.; Akbarov, R.; Nuruyev, S.; Sadigov, A.; Mammadli, A.; Mammadov, R.; Kopatch, Y.; Pridal, P.; Yilmaz, E.; Doganci, E.; Zich, J. Gamma-Ray Spectroscopy with MAPD Array in the Readout of LaBr3:Ce Scintillator. *J. Instrum.* **2021**, *16* (7), P07020. https://doi.org/10.1088/1748-0221/16/07/P07020

Blasse, G. Scintillator Materials. *Chem. Mater.* **1994**, *6* (9), 1465–1475. https://doi.org/10.1021/cm00045a002

Blasse, G.; Grabmaier, B. C. A General Introduction to Luminescent Materials. In *Luminescent Materials*; Springer Berlin Heidelberg: Berlin, Heidelberg, 1994; pp 1–9. https://doi.org/10.1007/978-3-642-79017-1_1

Boukerika, A.; Guerbous, L. Annealing Effects on Structural and Luminescence Properties of Red $Eu^{3+}$-Doped $Y_2O_3$ Nanophosphors Prepared by Sol–Gel Method. *J. Lumin.* **2014**, *145*, 148–153. https://doi.org/10.1016/j.jlumin.2013.07.037

Buijs, M.; Meyerink, A.; Blasse, G. Energy Transfer between Eu3+ Ions in a Lattice with Two Different Crystallographic Sites: $Y_2O_3$:$Eu^{3+}$, $Gd_2O_3$:$Eu^{3+}$ and $Eu_2O_3$. *J. Lumin.* **1987**, *37* (1), 9–20. https://doi.org/10.1016/0022-2313(87)90177-3

Cebim, M. A.; Souza Oliveira, H. H.; Barelli, N.; Davolos, M. R. System for X-Ray Excited Optical Luminescence (XEOL) Measurements. *Quim. Nova*. **2011**, *34* (6), 1057–1062. https://doi.org/10.1590/S0100-40422011000600024

Chen, Z. M.; Jiang, S. X.; Guo, R. H.; Xin, B. J.; Miao, D. G. Microstructure and Photoluminescent Properties of $Y_2O_3$:$Eu^{3+}$ Phosphors Synthesised by Precipitation and Combustion Methods. *Mater. Technol.* **2014**, *29* (4), 198–203. https://doi.org/10.1179/1753555713Y.0000000123

Dorenbos, P. The $Eu^{3+}$ Charge Transfer Energy and the Relation with the Band Gap of Compounds. *J. Lumin.* **2005**, *111* (1–2), 89–104. https://doi.org/10.1016/j.jlumin.2004.07.003

Dorenbos, P. Systematic Behaviour in Trivalent Lanthanide Charge Transfer Energies. *J. Phys. Condens. Matter*. **2003**, *15* (49), 8417–8434. https://doi.org/10.1088/0953-8984/15/49/018

Dujardin, C.; Auffray, E.; Bourret-Courchesne, E.; Dorenbos, P.; Lecoq, P.; Nikl, M.; Vasil'ev, A. N.; Yoshikawa, A.; Zhu, R.-Y. Needs, Trends, and Advances in Inorganic Scintillators. *IEEE Trans. Nucl. Sci.* **2018**, *65* (8), 1977–1997. https://doi.org/10.1109/TNS.2018.2840160

Ezirmik, K. V. Concentration Quenching of Photoluminescence in Optically Transparent $Lu_2O_3$:Eu Thin Films Deposited to Be Used as Scintillators. *Mater. Res. Express*. **2021**, *8* (1), 016407. https://doi.org/10.1088/2053-1591/abda64

Ferrari, J. L.; Cebim, M. A.; Pires, A. M.; Couto dos Santos, M. A.; Davolos, M. R. $Y_2O_3$:$Eu^{3+}$ (5 mol%) with Ag Nanoparticles Prepared by Citrate Precursor. *J. Solid State Chem.* **2010**, *183* (9), 2110–2115. https://doi.org/10.1016/j.jssc.2010.07.010

Gaspar, R. D. L.; Mazali, I. O.; Sigoli, F. A. Particle Size Tailoring and Luminescence of Europium(III)-Doped Gadolinium Oxide Obtained by the Modified Homogeneous Precipitation Method: Dielectric Constant and Counter Anion Effects. *Colloids Surfaces A Physicochem. Eng. Asp.* **2010**, *367* (1–3), 155–160. https://doi.org/10.1016/j.colsurfa.2010.07.003

Joffin, N.; Dexpert-Ghys, J.; Verelst, M.; Baret, G.; Garcia, A. The Influence of Microstructure on Luminescent Properties of :Eu Prepared by Spray Pyrolysis. *J. Lumin.* **2005**, *113* (3–4), 249–257. https://doi.org/10.1016/j.jlumin.2004.10.021

Jørgensen, C. K. *Modern Aspects of Ligand Field Theory*; North-Holland Publishing Company: Amsterdam, 1971.

Khachatourian, A. M.; Golestani-Fard, F.; Sarpoolaky, H.; Vogt, C.; Vasileva, E.; Mensi, M.; Popov, S.; Toprak, M. S. Microwave Synthesis of $Y_2O_3$:$Eu^{3+}$ Nanophosphors: A Study on the Influence of Dopant Concentration and Calcination Temperature on Structural and Photoluminescence Properties. *J. Lumin.* **2016**, *169*, 1–8. https://doi.org/10.1016/j.jlumin.2015.08.059

Khan, S.; Choi, Y.; Ahn, H.-Y.; Han, J. H.; Ju, B.-K.; Chung, J.; Cho, S.-H. Control of Particle Size in Flame Spray Pyrolysis of Tb–Doped $Y_2O_3$ for Bio-Imaging. *Materials (Basel).* **2020**, *13* (13), 2987. https://doi.org/10.3390/ma13132987

Khan, S.; Han, J. S.; Lee, S. Y.; Cho, S.-H. Flame-Synthesized $Y_2O_3$:$Tb^{3+}$ Nanocrystals as Spectral Converting Materials. *J. Nanoparticle Res.* **2018**, *20* (9), 241. https://doi.org/10.1007/s11051-018-4347-7

Levy, M. R.; Stanek, C. R.; Chroneos, A.; Grimes, R. W. Defect Chemistry of Doped Bixbyite Oxides. *Solid State Sci.* **2007**, *9* (7), 588–593. https://doi.org/10.1016/j.solidstatesciences.2007.02.009

Lu, B.; Li, J.-G.; Sakka, Y. Controlled Processing of $(Gd,Ln)_2O_3$:Eu (Ln = Y, Lu) Red Phosphor Particles and Compositional Effects on Photoluminescence. *Sci. Technol. Adv. Mater.* **2013**, *14* (6), 064202. https://doi.org/10.1088/1468-6996/14/6/064202

Malek Khachatourian, A.; Golestani-Fard, F.; Sarpoolaky, H.; Vogt, C.; Toprak, M. S. Microwave Assisted Synthesis of Monodispersed $Y_2O_3$ and $Y_2O_3$:$Eu^{3+}$ Particles. *Ceram. Int.* **2015**, *41* (2), 2006–2014. https://doi.org/10.1016/j.ceramint.2014.09.105

Mukherjee, S.; Sudarsan, V.; Vatsa, R. K.; Godbole, S. V; Kadam, R. M.; Bhatta, U. M.; Tyagi, A. K. Effect of Structure, Particle Size and Relative Concentration of Eu3+ and Tb3+ Ions on the Luminescence Properties of $Eu^{3+}$ Co-Doped $Y_2O_3$:Tb Nanoparticles. *Nanotechnology*. **2008**, *19* (32), 325704. https://doi.org/10.1088/0957-4484/19/32/325704

Nakamoto, K. *Infrared and Raman Spectra of Inorganic and Coordination Compounds: Part B: Applications in Coordination, Organometallic, and Bioinorganic Chemistry*, 6th ed.; Wiley-Interscience: Hoboken, 2009.

Park, S. J.; Park, J. Y.; Yang, H. K. Multi Modality of Hollow Tube $Gd_2O_3$:$Eu^{3+}$ Nanoparticles by Using Nonpolar Solvent. *J. Alloys Compd.* **2017**, *725*, 807–817. https://doi.org/10.1016/j.jallcom.2017.07.245

Pechini, M. P. Method of Preparing Lead and Alkaline Earth Titanates and Niobates and Coating Method Using the Same to Form a Capacitor. US Patent No. 3330697, 1967. https://patentimages.storage.googleapis.com/72/c2/eb/b008578cda0646/US3330697.pdf

Pires, A. M.; Davolos, M. R.; Malta, O. L. $Eu^{3+}$-$O_2$− Associates Luminescence in Ba2SiO4. *J. Lumin.* **1997**, *72–74*, 244–246. https://doi.org/10.1016/S0022-2313(96)00357-2

Pires, A. M.; Davolos, M. R.; Stucchi, E. B. $Eu^{3+}$ as a Spectroscopic Probe in Phosphors Based on Spherical Fine Particle Gadolinium Compounds. *Int. J. Inorg. Mater.* **2001**, *3* (7), 785–790. https://doi.org/10.1016/S1466-6049(01)00041-1

Pires, A.; Santos, M.; Davolos, M.; Stucchi, E. The Effect of $Eu^{3+}$ Ion Doping Concentration in $Gd_2O_3$ Fine Spherical Particles. *J. Alloys Compd.* **2002**, *344* (1–2), 276–279. https://doi.org/10.1016/S0925-8388(02)00368-7

Pires, A. M.; Davolos, M. R.; Paiva-Santos, C. O.; Stucchi, E. B.; Flor, J. New X-Ray Powder Diffraction Data and Rietveld Refinement for $Gd_2O_3$ Monodispersed Fine Spherical Particles. *J. Solid State Chem.* **2003**, *171* (1–2), 420–423. https://doi.org/10.1016/S0022-4596(02)00224-4

Shang, C.; Shang, X.; Qu, Y.; Li, M. Investigation on the Red Shift of Charge Transfer Excitation Spectra for Nano-Sized $Y_2O_3$:$Eu^{3+}$. *Chem. Phys. Lett.* **2011**, *501* (4–6), 480–484. https://doi.org/10.1016/j.cplett.2010.11.085

Srinivasan, R.; Yogamalar, N. R.; Elanchezhiyan, J.; Joseyphus, R. J.; Bose, A. C. Structural and Optical Properties of Europium Doped Yttrium Oxide Nanoparticles for Phosphor Applications. *J. Alloys Compd.* **2010**, *496* (1–2), 472–477. https://doi.org/10.1016/j.jallcom.2010.02.083

Srinivasan, R.; Yogamalar, R.; Bose, A. C. Structural and Optical Studies of Yttrium Oxide Nanoparticles Synthesized by Co-Precipitation Method. *Mater. Res. Bull.* **2010**, *45* (9), 1165–1170. https://doi.org/10.1016/j.materresbull.2010.05.020

Stanek, C. R.; Levy, M. R.; McClellan, K. J.; Uberuaga, B. P.; Grimes, R. W. Defect Identification and Compensation in Rare Earth Oxide Scintillators. *Nucl. Instruments Methods Phys. Res. Sect. B Beam Interact. with Mater. Atoms*. **2008**, *266* (12–13), 2657–2664. https://doi.org/10.1016/j.nimb.2008.03.209

Sun, Y; Qi, L; Lee, M; Lee, B. I; Samuels, W. D; Exarhos, G. J. Photoluminescent Properties of $Y_2O_3$:$Eu^{3+}$ Phosphors Prepared via Urea Precipitation in Non-Aqueous Solution. *J. Lumin.* **2004**, *109* (2), 85–91. https://doi.org/10.1016/j.jlumin.2004.01.085

Tomala, R.; Strek, W. Influence of Graphene Flakes on Upconversion Spectra of $Y_2O_3$:$Yb^{3+}$,$Er^{3+}$ Nanocrystalline Powders. *Opt. Mater. (Amst).* **2020**, *109*, 110047. https://doi.org/10.1016/j.optmat.2020.110047

Wang, W.-N.; Widiyastuti, W.; Ogi, T.; Lenggoro, I. W.; Okuyama, K. Correlations between Crystallite/Particle Size and Photoluminescence Properties of Submicrometer Phosphors. *Chem. Mater.* **2007**, *19* (7), 1723–1730. https://doi.org/10.1021/cm062887p

Wu, X.; Liang, Y.; Liu, R.; Li, Y. The Photoluminescence Properties of $Y_2O_3$:$Eu^{3+}$ Prepared by Surfactant Assisted Co-Precipitation-Molten Salt Synthesis. *Mater. Res. Bull.* **2010**, *45* (5), 594–597. https://doi.org/10.1016/j.materresbull.2010.01.012

Yousif, A.; Abas, B. H.; Som, S.; Shivaramu, N. J.; Swart, H. C. Structural and Luminescence Properties of $Y_2O_3$:$Eu^{3+}$ red Phosphor by Incorporation of $Ga^{3+}$ and $Bi^{3+}$ ions. *Mater. Res. Bull.* **2020**, *124*, 110752. https://doi.org/10.1016/j.materresbull.2019.110752

Zhou, F.; Li, Z.; Lan, W.; Wang, Q.; Ding, L.; Jin, Z. Halide Perovskite, a Potential Scintillator for X-Ray Detection. *Small Methods*. **2020**, *4* (10). https://doi.org/10.1002/smtd.202000506

Zhou, J.; Leaño, J. L.; Liu, Z.; Jin, D.; Wong, K.; Liu, R.; Bünzli, J. G. Impact of Lanthanide Nanomaterials on Photonic Devices and Smart Applications. *Small*. **2018**, *14* (40). https://doi.org/10.1002/smll.201801882